Overall Water Splitting

International Edition: DOI: 10.1002/anie.201602237
German Edition: DOI: 10.1002/ange.201602237

Interface Engineering of MoS_2/Ni_3S_2 Heterostructures for Highly Enhanced Electrochemical Overall-Water-Splitting Activity

*Jian Zhang, Tao Wang, Darius Pohl, Bernd Rellinghaus, Renhao Dong, Shaohua Liu, Xiaodong Zhuang, and Xinliang Feng**

Abstract: *To achieve sustainable production of H_2 fuel through water splitting, low-cost electrocatalysts for the hydrogen-evolution reaction (HER) and the oxygen-evolution reaction (OER) are required to replace Pt and IrO_2 catalysts. Herein, for the first time, we present the interface engineering of novel MoS_2/Ni_3S_2 heterostructures, in which abundant interfaces are formed. For OER, such MoS_2/Ni_3S_2 heterostructures show an extremely low overpotential of ca. 218 mV at 10 mA cm^{-2}, which is superior to that of the state-of-the-art OER electrocatalysts. Using MoS_2/Ni_3S_2 heterostructures as bifunctional electrocatalysts, an alkali electrolyzer delivers a current density of 10 mA cm^{-2} at a very low cell voltage of ca. 1.56 V. In combination with DFT calculations, this study demonstrates that the constructed interfaces synergistically favor the chemisorption of hydrogen and oxygen-containing intermediates, thus accelerating the overall electrochemical water splitting.*

To achieve sustainable hydrogen production, electrochemical and photoelectrochemical water splitting are favorable strategies benefiting from abundant water resources and giving high-purity H_2 production.[1] Electrocatalysts are particularly vital to the hydrogen-evolution reaction (HER) and the oxygen-evolution reaction (OER) by lowering the dynamic overpotentials.[2] Currently, Pt is the most efficient HER electrocatalyst with a near-zero overpotential, while IrO_2 and RuO_2 hold the benchmark for OER electrocatalysts.[3] However, the scarcity and high-cost of these noble-metal-based electrocatalysts considerably impede their large-scale utilization in commercial electrolyzers.[4] For the HER in an alkaline solution, the kinetics are determined through a subtle balance between the water dissociation (Volmer step) and the subsequent chemisorption of the water-splitting intermediates (OH^- and H*) on the surface of the HER electrocatalyst.[5] Thus, once an electrocatalyst facilitates the synergistic chemisorption of both H* and OH^- intermediates on the surface, the HER performance will be improved. Similarly, for the OER in an alkaline solution, the chemisorption and dissociation of OH^- and the yielded intermediates (OH*, OOH*, and H^+) on the surface of the electrocatalysts determine the water-oxidation activity.[6] Therefore, OER electrocatalysts capable of binding both the oxygen-containing and hydrogen intermediates are expected to favor the water-oxidation reaction. Nevertheless, only the chemisorption free energy of hydrogen (or oxygen-containing) intermediates has been considered for developing HER (or OER) electrocatalysts thus far.[7]

Molybdenum-based nanostructures, particularly MoS_2, have been extensively investigated as HER electrocatalysts.[8] Both DFT calculations and experimental investigations revealed that the undercoordinated Mo-S sites along the edges of MoS_2 possess high chemisorption capability for hydrogen, analogous to Pt.[9] For OER electrocatalysts earth-abundant transition-metal (Fe, Co, and Ni, particularly Ni)-based sulfides,[10] oxides,[11] hydroxides,[12] layered double hydroxides (LDHs),[13] and phosphates[14] have been explored. The undercoordinated metal sites on the surface are pivotal in water oxidation because of their outstanding chemisorption of OH^- and oxygen-containing intermediates. Therefore, integrating the advantages of the HER and OER electrocatalysts to construct novel heterostructures, which possess binding affinities to both hydrogen and oxygen-containing intermediates, is extremely beneficial for enhancing the overall electrochemical water-splitting activity.

Herein, for the first time, we present the interface engineering of novel MoS_2/Ni_3S_2 heterostructures on nickel foam. In the resultant MoS_2/Ni_3S_2 heterostructures, the outer MoS_2 nanosheets are decorated on the surface of the inner Ni_3S_2 nanoparticles, which generates abundant interfaces. Such MoS_2/Ni_3S_2 heterostructures exhibit both highly efficient OER and HER activities in 1 M KOH solution. In particular, the OER onset potential of MoS_2/Ni_3S_2 heterostructures is as low as around 175 mV, and the OER current density reaches 10 mA cm^{-2} at an overpotential of about 218 mV, which is superior to the reported OER electrocatalysts. Furthermore, utilizing the MoS_2/Ni_3S_2 heterostructure as a bifunctional electrocatalyst, an alkaline electrolyzer with a current density of 10 mA cm^{-2} is operated at a low cell voltage of 1.56 V, which is considerably lower than that of the state-of-the-art overall-water-splitting electrocatalysts, such as NiFe–LDH,[15] NiSe nanowires,[16] Ni_2P nanoparticles,[17] and electrodeposited cobalt-phosphorous-derived films[18] (cell voltages >1.6 V). Combined with DFT calculations, our results suggest that the established interfaces between

[*] Dr. J. Zhang, Dr. R. Dong, Dr. S. Liu, Dr. X. Zhuang, Prof. X. Feng
Center for Advancing Electronics Dresden (cfaed) & Department of Chemistry and Food Chemistry
Technische Universität Dresden
01062 Dresden (Germany)
E-mail: xinliang.feng@tu-dresden.de
Dr. T. Wang
Leibniz-Institut für Katalyse, e.V., Universität Rostock
18059 Rostock (Germany)
Dr. D. Pohl, Dr. B. Rellinghaus
Institute for Metallic Materials, IFW Dresden
01171 Dresden (Germany)

Supporting information for this article can be found under: http://dx.doi.org/10.1002/anie.201602237.

Ni_3S_2 and MoS_2 as well as the in situ generated interfaces between NiO (surface electrochemical oxidation of Ni_3S_2 under OER condition) and MoS_2 facilitate the synchronous chemisorption of hydrogen and oxygen-containing intermediates, consequently improving the overall electrochemical water-splitting activity.

MoS_2/Ni_3S_2 heterostructures were prepared using a commercial nickel foam ($1 \times 3\ cm^2$) and $(NH_4)_2MoS_4$ (40 mg) through a one-pot solvothermal reaction at 200 °C for 12 h in 15 mL *N*,*N*-dimethylformamide (DMF; see Supporting Information). During the solvothermal reaction, $(NH_4)_2MoS_4$ not only served as the precursor of MoS_2 nanosheets but also provided the sulfur source for the in situ growth of Ni_3S_2 nanoparticles on the nickel foam. The loading amount of MoS_2/Ni_3S_2 heterostructures on the nickel foam is approximately 9.7 $mg\,cm^{-2}$; this value could be controlled by adjusting the amount of $(NH_4)_2MoS_4$ in the solution. For instance, the loading weights of MoS_2/Ni_3S_2 heterostructures were approximately 5.7 and approximately 13.1 $mg\,cm^{-2}$ when the amounts of $(NH_4)_2MoS_4$ were 20 and 80 mg, respectively (Figure S1–S3 in the Supporting Information).

As shown in Figure 1 a and the inset, the resulting nickel foam coated with MoS_2/Ni_3S_2 heterostructures has macroporous and free-standing features. The crystalline structure and surface composition of the MoS_2/Ni_3S_2 heterostructures were first confirmed through X-ray diffraction (Figure S4) and Raman spectroscopy (Figure S5) studies. To analyze the as-obtained MoS_2/Ni_3S_2 heterostructures, scanning electron microscopy (SEM) and high-resolution transmission electron microscopy (HRTEM) were used. Figure 1 b reveals numerous heterostructures, which consist of inner Ni_3S_2 nanoparticles and decorated MoS_2 nanosheets. The size of the Ni_3S_2 nanoparticles was about several hundred nanometers. The size and thickness of the MoS_2 nanosheets were 30–130 and 5–15 nm, respectively. The element distributions of the MoS_2/Ni_3S_2 heterostructures were further analyzed through the elemental mapping of field-emission SEM (FE-SEM) (Figure S6 a–d). Notably, the nickel element was mainly distributed over the nanoparticles, whereas molybdenum and sulfur were spread on and around the nanoparticles. The molar content of MoS_2 in MoS_2/Ni_3S_2 heterostructures was determined to be about 7.8 % through energy-dispersive X-ray spectroscopy (EDX) (Figure S6 e), which is consistent with the inductively coupled plasma mass spectrometer (ICP-MS) analysis (ca. 8.0 %). We further peeled off MoS_2/Ni_3S_2 heterostructures from the nickel foam by sonication and investigated the samples by HRTEM (Figure 1 c, 1 d, S7 and S8). Lattice fringes with lattice distances of 0.27 and 0.61 nm corresponded to the (100) and (002) facets of MoS_2, respectively, while the lattice distances of 0.40 and 0.28 nm were ascribed to the (101) and (110) facets of Ni_3S_2, respectively. The (002) and (100) facets of MoS_2 and the neighboring (101) and (110) surfaces of Ni_3S_2 constitute the interfaces in MoS_2/Ni_3S_2 heterostructures. Next, the X-ray photoelectron spectroscopy (XPS) survey spectrum of MoS_2/Ni_3S_2 demonstrates that the chemical composition of Ni, Mo, and S is consistent with the EDX results (Figure S9). For bare MoS_2 nanosheets, the peaks of Mo $3d_{5/2}$ and Mo $3d_{3/2}$ appear at 228.5 and 231.8 eV, respectively. However, the binding energies of Mo $3d_{5/2}$ and Mo $3d_{3/2}$ in MoS_2/Ni_3S_2 heterostructures shift to 228.6 and 232.2 eV, respectively (Figure 1 e). Similarly, the Ni $2p_{3/2}$ signal in the MoS_2/Ni_3S_2 heterostructures exhibits a positive shift of about 0.3 eV relative to that in the bare Ni_3S_2 nanoparticles (Figure 1 f). These results strongly suggest the existence of strong electronic interactions between Ni_3S_2 and MoS_2, which implies the establishment of coupling interfaces.

To evaluate the OER performance of the as-prepared MoS_2/Ni_3S_2 heterostructures, a three-electrode configuration was applied using an Hg/HgO electrode and a Pt rod as the reference and counter electrodes, respectively (Figure S10). The OER activities of the nickel foam, Ni_3S_2 nanoparticles, MoS_2 nanosheets, MoS_2/Ni_3S_2 heterostructures, and IrO_2 were examined through cyclic voltammetry (CV) at a scan rate of 1 $mV\,s^{-1}$ in a 1 M KOH aqueous solution purged with O_2 (Figure 2 a). Bare Ni_3S_2 nanoparticles and MoS_2 nanosheets exhibited OER onset overpotentials of approximately 230 and 280 mV, respectively. By contrast, for MoS_2/Ni_3S_2 heterostructures, oxygen generation occurred at an extremely low overpotential (ca. 175 mV), which is considerably lower than that of commercial IrO_2 (ca. 250 mV) (Figure S11 and S12). Significantly, the current density of MoS_2/Ni_3S_2 heterostructures reached 10 $mA\,cm^{-2}$ at an extremely low overpotential of approximately 218 mV, which outperformed IrO_2 (ca. 330 mV) and the NiFe-LDH film (ca.

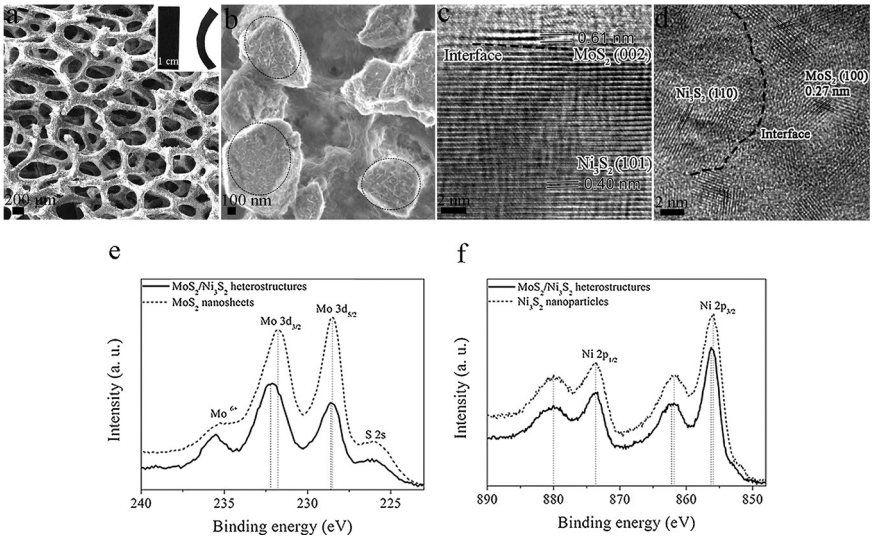

Figure 1. a) and b) scanning electron microscopy and c) and d) high-resolution transmission electron microscopy images of MoS_2/Ni_3S_2 heterostructures. High-resolution X-ray photoelectron spectroscopy spectrum of e) Mo 3d and f) Ni 2p. Inset of (a): digital image of nickel foam coated with MoS_2/Ni_3S_2 heterostructures. The ringed sections of (b) highlight the MoS_2 nanosheets.

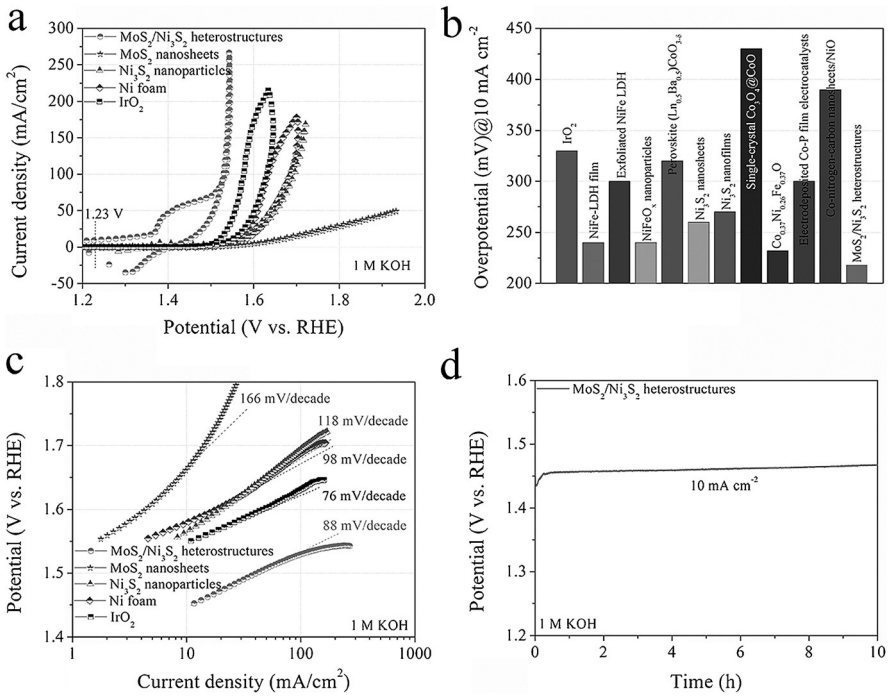

Figure 2. a) CV curves and c) related Tafel slopes of the nickel foam, MoS_2 nanosheets, Ni_3S_2 nanoparticles, MoS_2/Ni_3S_2 heterostructures, and IrO_2; b) OER overpotentials of the MoS_2/Ni_3S_2 heterostructures and the reported electrocatalysts for comparison at 10 mA cm^{-2}; and d) the long-term electrochemical OER test of the MoS_2/Ni_3S_2 heterostructures at 10 mA cm^{-2}. Electrolyte: 1 M KOH solution; CV scan rate: 1 mV s^{-1}.

240 mV),[15] $(Ln_{0.5}Ba_{0.5})CoO_{3-\delta}$ perovskite (ca. 320 mV),[19] single-crystal Co_3O_4@CoO (ca. 430 mV),[20] and electrodeposited Co-P film (ca. 300 mV)[19] (Figure 2b).[10,21]

Figure 2c illustrates that the Tafel slope of the MoS_2/Ni_3S_2 heterostructures is approximately 88 mV decade^{-1}, which is considerably lower than that of the Ni_3S_2 nanoparticles (ca. 118 mV decade^{-1}), the MoS_2 nanosheets (ca. 166 mV decade^{-1}), and the nickel foam (ca. 98 mV decade^{-1}). This result strongly suggests that the MoS_2/Ni_3S_2 heterostructures activate water-oxidation reaction kinetics.

To assess the electrochemical OER stability of MoS_2/Ni_3S_2 heterostructures, a long-term water oxidation was conducted at 10 mA cm^{-2} in 1 M KOH media. Figure 2d illustrates that the MoS_2/Ni_3S_2 heterostructures retained steady OER activity and no noticeable potential augment was observed for more than 10 h of oxygen release.

The HER activities of the as-prepared samples were evaluated in 1 M KOH electrolyte purged with N_2. The polarization curves in Figure 3a show that the onset overpotentials of Ni_3S_2 nanoparticles and MoS_2 nanosheets are approximately 120 and 236 mV, respectively. However, the onset overpotential of the MoS_2/Ni_3S_2 heterostructures is substantially lower at around 50 mV, approaching that of the Pt catalyst. At 10 mA cm^{-2}, the applied overpotential is approximately 110 mV, substantially lower than that of the Ni_3S_2 nanoparticles (ca. 193 mV), the MoS_2 nanosheets (ca. 431 mV), and the recently reported WC nanocrystals on carbon nanotubes (ca. 150 mV),[22] CoP on carbon cloth (ca. 209 mV),[23] MoC_x nano-octahedrons (ca. 150 mV),[24] and cobalt-nitrogen-rich carbon nanotubes (ca. 360 mV)[25] (Figures S13,S14). The Tafel slopes of the MoS_2/Ni_3S_2 heterostructures, Ni_3S_2 nanoparticles, and MoS_2 nanosheets are around 83, 85, and 308 mV per decade, respectively (Figure 3b). Such a Tafel slope of the MoS_2/Ni_3S_2 heterostructures suggests a combined Volmer–Heyrovsky mechanism for hydrogen production.[26] Under a cathodic current of 10 mA cm^{-2},

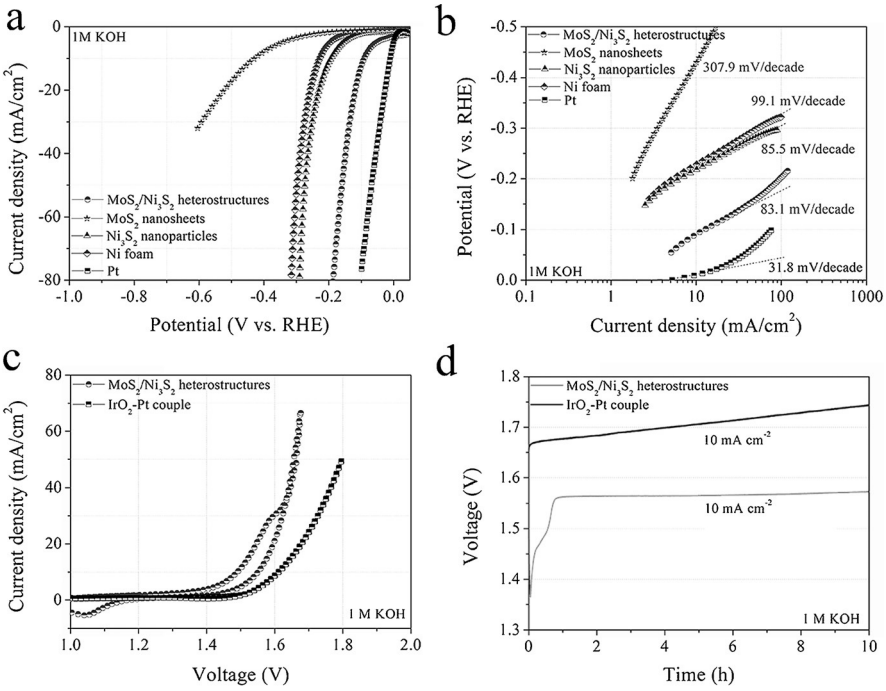

Figure 3. a) Polarization curves and b) corresponding Tafel slopes of the nickel foam, MoS_2 nanosheets, Ni_3S_2 nanoparticles, MoS_2/Ni_3S_2 heterostructures, and Pt; c) polarization curves of MoS_2/Ni_3S_2 heterostructures and IrO_2-Pt couple in a two-electrode system; and d) durable operation of the MoS_2/Ni_3S_2 (lower trace) heterostructures and IrO_2-Pt couple (upper trace) at 10 mA cm^{-2} in an alkaline electrolyzer. Electrolyte: 1 M KOH solution; CV scan rate: 1 mV s^{-1}.

there is no noticeable degradation over a 10 h galvanostatic test, which indicates an excellent electrochemical HER stability (Figure S15).

The MoS_2/Ni_3S_2 heterostructures were utilized as a bifunctional electrocatalyst for overall water splitting in a two-electrode setup in 1M KOH solution (Figure S16). A current density of 10 mA cm^{-2} was delivered at approximately 1.56 V, that is, a combined overpotential of about 330 mV for electrochemical overall water splitting (Figure 3c). Figure S17 reveals that the overall water splitting activity of the MoS_2/Ni_3S_2 heterostructures is much higher than that of the IrO_2-Pt couple (ca. 1.7 V) and other recently reported overall water splitting electrocatalysts such as NiFe-LDH (ca. 1.7 V),[16] NiSe nanowires (ca. 1.63 V),[17] and Ni_2P nanoparticles (ca. 1.63 V).[18] Over a 10 h galvanostatic electrolysis at 10 mA cm^{-2}, the MoS_2/Ni_3S_2 heterostructures presented an excellent durability with negligible degradation, which is superior to that of the noble metal IrO_2-Pt couple (Figure 3d). We further tested the overall electrocatalytic water splitting performance under an extremely high current density of 500 mA cm^{-2}. Figure S18 and Movie 1 show that massive bubbles were rapidly generated on both electrodes at an applied voltage of approximately 1.6 V. Such a prominent performance of the constructed electrolyzer utilizing the MoS_2/Ni_3S_2 heterostructures is close to the commercial requirement of a water splitting electrolyzer (voltage $\leq$ 1.55 V at 500 mA cm^{-2}).[27]

The nature and amount of undercoordinated metal sites are crucial for the electrochemical water splitting. The effects of the surface area on OER and HER activities of the obtained-electrocatalysts were firstly studied through electrochemical double-layer capacitances (C_{dl}; Figure S19). As shown in Table S1, MoS_2/Ni_3S_2 heterostructures show a larger C_{dl} (15.6 mF) than Ni_3S_2 nanoparticles (2.1 mF) and MoS_2 nanosheets (8.2 mF). In sharp contrast, for OER (or HER), the current density of MoS_2/Ni_3S_2 heterostructures at 1.53 V (or −0.15 V) reached 94.8 (or 45) mA cm^{-2}, which is substantially higher than those of Ni_3S_2 nanoparticles (5.0 mA cm^{-2} for OER; 4.7 mA cm^{-2} for HER) and MoS_2 nanosheets (1.6 mA cm^{-2} for OER; 2.5 mA cm^{-2} for HER). Thereby, the greatly enhanced water splitting activities of MoS_2/Ni_3S_2 heterostructures are mainly attributed to the constructed interfaces, rather than the active surface areas.

As shown in Figure S20, the reduction and oxidation peaks of $Mo^{\delta+}/Mo^{\varepsilon+}$ ($\varepsilon > \delta \geq 4$) in MoS_2 nanosheets are located at ≈0.333 and 0.449 V, while the redox reactions of Ni^{2+}/Ni^{3+} in Ni_3S_2 nanoparticles occur at around 0.254 and 0.369 V. In contrast, the redox peaks in the MoS_2/Ni_3S_2 heterostructures are centered at about 0.216 and 0.489 V. These results suggest that the fabricated MoS_2/Ni_3S_2 heterostructures offer new water splitting active sites, which are endowed with the electrocatalytic properties of both Ni_3S_2 and MoS_2. The reduction peak area of MoS_2/Ni_3S_2 heterostructures is approximately 9.3 and 17.7 times larger than those of the Ni_3S_2 nanoparticles and MoS_2 nanosheets, respectively. After the electrochemical OER process at 10 mA cm^{-2} for 10 h in 1M KOH solution, the structure of the MoS_2/Ni_3S_2 heterostructures was analyzed by SEM, HRTEM, XPS, element mapping and EDX, and XPS analyses (Figure S21–S24). Notably, a thin layer of NiO with thickness of approximately 12.6 nm was identified on Ni_3S_2 surface, for which the lattice fringe with a lattice distance of 0.21 nm was indexed to be the (010) facet of NiO (Figure S20c). XPS result in Figure S24 further revealed the existence of NiO. The formation of NiO is due to the in situ surface electrochemical oxidation of Ni_3S_2 during the OER process which is in agreement with literature reports; and the NiO sites are electrochemically active for the OER process.[10,16] Therefore, we consider that the constructed inter-

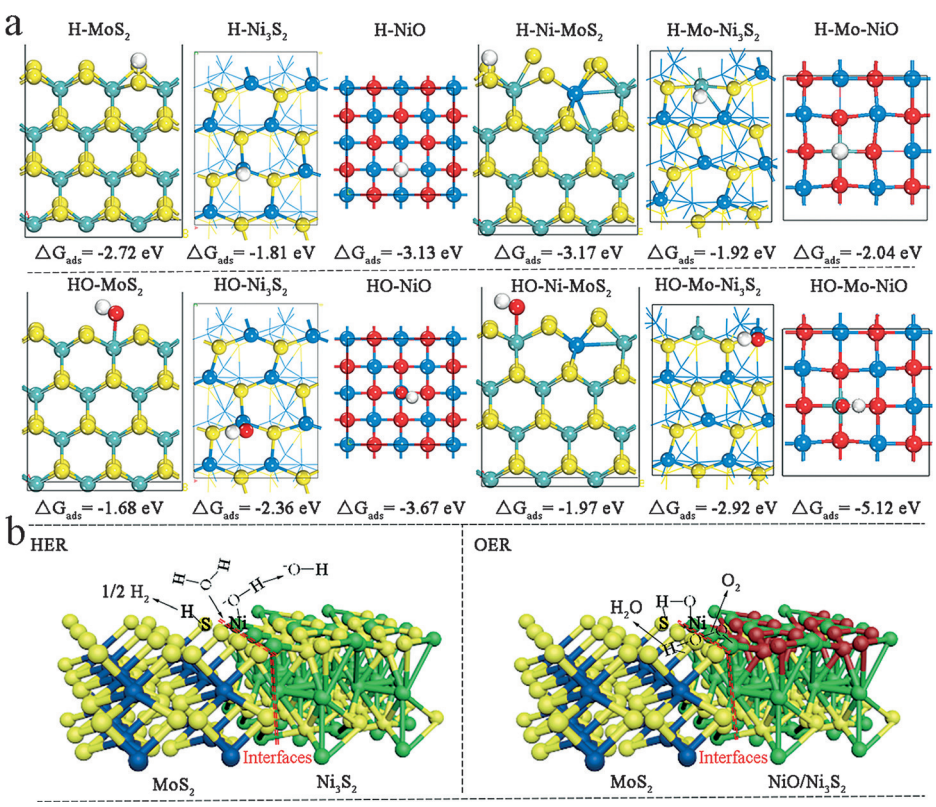

Figure 4. a) Chemisorption models of H and OH intermediates on the surfaces of MoS_2, Ni_3S_2, NiO, MoS_2/Ni_3S_2 heterostructures (Ni-MoS_2 and Mo-Ni_3S_2 models), and MoS_2/NiO heterostructures (Ni-MoS_2 and Mo-NiO models) respectively; b) the proposed mechanisms of the dissociation of H_2O, OH, and OOH intermediates on the MoS_2/Ni_3S_2 heterostructures. Yellow = S, green = Ni, blue = Mo, white = H, red = O

faces between the Ni_3S_2 and MoS_2 stably facilitate HER process and the interfaces between the in situ formed NiO and MoS_2 are favorable for the OER process.

To further investigate the role of the constructed interfaces in electrochemical OER and HER, the MoS_2/Ni_3S_2 heterostructures with different molar contents of MoS_2 have been synthesized on carbon cloth (see Experimental Section in Supporting Information). Figure S25 shows that the OER and HER overpotentials of the bare Ni_3S_2 nanoparticles and MoS_2 nanosheets at 10 mA cm^{-2} are approximately 379 and 421 and 341 and 429 mV, respectively. However, the electrochemical OER and HER performances of the MoS_2/Ni_3S_2 heterostructures are noticeably enhanced. When the molar content of MoS_2 is around 8.3%, the OER and HER overpotentials of the MoS_2/Ni_3S_2 heterostructures at 10 mA cm^{-2} are as low as approximately 330 and 150 mV, respectively. For comparison, the physically mixed MoS_2/Ni_3S_2 composite (having the same chemical composition as the MoS_2/Ni_3S_2 heterostructures) deliver OER and HER current densities of 10 mA cm^{-2} at overpotentials of about 356 and 199 mV, respectively, which are considerably higher than those of the MoS_2/Ni_3S_2 heterostructures. These results clearly show the crucial role of the constructed interfaces between Ni_3S_2 and MoS_2 as well as the interfaces between NiO and MoS_2, which are responsible for the enhanced electrochemical hydrogen and oxygen evolutions, respectively.

To clarify the effect of the constructed interfaces on the chemisorption of hydrogen and oxygen-containing intermediates, we utilized DFT to calculate the chemisorption free energies of hydrogen (ΔG_H) and hydroxide (ΔG_{OH}) on the (101) surface of Ni_3S_2, the (010) surface of NiO, and the (002) surface of MoS_2 (Figure 4a). Contrary to the chemisorption on the (101) surface of Ni_3S_2 ($\Delta G_H = -1.81$ eV) and (002) surface of MoS_2 ($\Delta G_H = -2.71$ eV), H is prone to adsorb on the Mo-S edge sites of Ni-doped MoS_2 model (denoted as Ni-MoS_2) because of a lower chemisorption free energy of −3.17 eV. As expected, the surface undercoordinated Ni sites of Mo-doped Ni_3S_2 model (denoted as Mo-Ni_3S_2) have a HO-chemisorption energy of −2.92 eV, which is lower than the −1.68 eV energy of HO-chemisorption on MoS_2 and −2.36 eV energy of Ni_3S_2. The (101) surface of Mo-Ni_3S_2 thus exhibits superior binding activity toward oxygen-containing groups. Moreover, considering the formed interfaces between MoS_2 and NiO for OER, the Mo sites of the Mo-doped NiO model (Mo-NiO) show a significantly increased HO-chemisorption energy up to −5.12 eV. Accordingly, a HER mechanism on MoS_2/Ni_3S_2 heterostructures and an OER mechanism on MoS_2/NiO heterostructures are proposed in Figure 4b. The constructed interfaces between Ni_3S_2 and MoS_2 as well as the interfaces between NiO and MoS_2 have the advantages of the H-chemisorption of MoS_2 and the HO-chemisorption of Ni_3S_2 and NiO. As a result, the Gibbs free energies of the corresponding intermediates are efficiently decreased, facilitating the dissociation of the O–H bonds of the H_2O molecule and the OH and OOH intermediates. Eventually, the OER and HER processes are highly accelerated.

In summary, we have presented a novel approach for developing earth-abundant and high-activity overall-water-splitting electrocatalysts through interface engineering. The as-prepared MoS_2/Ni_3S_2 heterostructures with abundant interfaces manifest excellent chemisorption abilities for both hydrogen and oxygen-containing intermediates, leading to outstanding OER and HER electrocatalytic activities in alkaline media. Therefore, the engineering and understanding of the interfaces formed provide a favorable direction for developing low-cost and high-activity water-splitting electrocatalysts, which have potential applications in photochemical, photoelectrochemical, and electrochemical H_2 production and CO_2 reduction.

Acknowledgements

This work was financially supported by the ERC Grant on 2DMATER and EC under Graphene Flagship (No. CNECT-ICT-604391). We also acknowledge the Cfaed (Center for Advancing Electronics Dresden) and the Dresden Center for Nanoanalysis (DCN) at TU Dresden.

Keywords: electrocatalysts · interface engineering · molybdenum disulfide · nickel sulfide · water splitting

How to cite: *Angew. Chem. Int. Ed.* **2016**, *55*, 6702–6707
Angew. Chem. **2016**, *128*, 6814–6819

[1] J. Greeley, T. F. Jaramillo, J. Bonde, I. Chorkendorff, J. K. Norskov, *Nat. Mater.* **2006**, *5*, 909–913.
[2] C. C. L. McCrory, S. Jung, I. M. Ferrer, S. M. Chatman, J. C. Peters, T. F. Jaramillo, *J. Am. Chem. Soc.* **2015**, *137*, 4347–4357.
[3] D. V. Esposito, S. T. Hunt, A. L. Stottlemyer, K. D. Dobson, B. E. McCandless, R. W. Birkmire, J. G. Chen, *Angew. Chem. Int. Ed.* **2010**, *49*, 9859–9862; *Angew. Chem.* **2010**, *122*, 10055–10058.
[4] K. Zeng, D. Zhang, *Prog. Energy Combust. Sci.* **2010**, *36*, 307–326.
[5] R. Subbaraman, D. Tripkovic, D. Strmcnik, K.-C. Chang, M. Uchimura, A. P. Paulikas, V. Stamenkovic, N. M. Markovic, *Science* **2011**, *334*, 1256–1260.
[6] I. C. Man, H. Y. Su, F. Calle-Vallejo, H. A. Hansen, J. I. Martínez, N. G. Inoglu, J. Kitchin, T. F. Jaramillo, J. K. Nørskov, J. Rossmeisl, *ChemCatChem* **2011**, *3*, 1159–1165.
[7] a) Y. Jiao, Y. Zheng, M. Jaroniec, S. Z. Qiao, *Chem. Soc. Rev.* **2015**, *44*, 2060–2086; b) J. Zhang, S. Liu, H. Liang, R. Dong, X. Feng, *Adv. Mater.* **2015**, *27*, 7426–7431; c) H.-W. Liang, S. Bruller, R. Dong, J. Zhang, X. Feng, K. Müllen, *Nat. Commun.* **2015**, *6*, 7992–7999; d) J. Wang, W. Cui, Q. Liu, Z. Xing, A. M. Asiri, X. Sun, *Adv. Mater.* **2016**, *28*, 215–230.
[8] Y. Yan, B. Xia, Z. Xu, X. Wang, *ACS Catal.* **2014**, *4*, 1693–1705.
[9] T. F. Jaramillo, K. P. Jørgensen, J. Bonde, J. H. Nielsen, S. Horch, I. Chorkendorff, *Science* **2007**, *317*, 100–102.
[10] W. Zhou, X.-J. Wu, X. Cao, X. Huang, C. Tan, J. Tian, H. Liu, J. Wang, H. Zhang, *Energy Environ. Sci.* **2013**, *6*, 2921–2924.
[11] R. D. L. Smith, M. S. Prévot, R. D. Fagan, Z. Zhang, P. A. Sedach, M. K. J. Siu, S. Trudel, C. P. Berlinguette, *Science* **2013**, *340*, 60–63.
[12] M. Gao, W. Sheng, Z. Zhuang, Q. Fang, S. Gu, J. Jiang, Y. Yan, *J. Am. Chem. Soc.* **2014**, *136*, 7077–7084.
[13] C. Tang, H.-S. Wang, H.-F. Wang, Q. Zhang, G.-L. Tian, J.-Q. Nie, F. Wei, *Adv. Mater.* **2015**, *27*, 4516–4522.
[14] M. W. Kanan, Y. Surendranath, D. G. Nocera, *Chem. Soc. Rev.* **2009**, *38*, 109–114.

[15] J. Luo, J.-H. Im, M. T. Mayer, M. Schreier, M. K. Nazeeruddin, N.-G. Park, S. D. Tilley, H. J. Fan, M. Grätzel, *Science* **2014**, *345*, 1593 – 1596.
[16] C. Tang, N. Cheng, Z. Pu, W. Xing, X. Sun, *Angew. Chem. Int. Ed.* **2015**, *54*, 9351 – 9355; *Angew. Chem.* **2015**, *127*, 9483 – 9487.
[17] L.-A. Stern, L. Feng, F. Song, X. Hu, *Energy Environ. Sci.* **2015**, *8*, 2347 – 2351.
[18] N. Jiang, B. You, M. Sheng, Y. Sun, *Angew. Chem. Int. Ed.* **2015**, *54*, 6251 – 6254; *Angew. Chem.* **2015**, *127*, 6349 – 6352.
[19] A. Grimaud, K. J. May, C. E. Carlton, Y.-L. Lee, M. Risch, W. T. Hong, J. Zhou, Y. Shao-Horn, *Nat. Commun.* **2013**, *4*, 2439 – 2445.
[20] C.-W. Tung, Y.-Y. Hsu, Y.-P. Shen, Y. Zheng, T.-S. Chan, H.-S. Sheu, Y.-C. Cheng, H. M. Chen, *Nat. Commun.* **2015**, *6*, 8106 – 8114.
[21] a) F. Song, X. Hu, *Nat. Commun.* **2014**, *5*, 4477 – 4485; b) H. Wang, H.-W. Lee, Y. Deng, Z. Lu, P.-C. Hsu, Y. Liu, D. Lin, Y. Cui, *Nat. Commun.* **2015**, *6*, 7261 – 7268; c) L.-L. Feng, G. Yu, Y. Wu, G.-D. Li, H. Li, Y. Sun, T. Asefa, W. Chen, X. Zou, *J. Am. Chem. Soc.* **2015**, *137*, 14023 – 14026; d) W. Chen, H. Wang, Y. Li, Y. Liu, J. Sun, S. Lee, J.-S. Lee, Y. Cui, *ACS Cent. Sci.* **2015**, *1*, 244 – 251; e) J. Wang, K. Li, H. - *x.* Zhong, D. Xu, Z.-l. Wang, Z. Jiang, Z.-j. Wu, X.-b. Zhang, *Angew. Chem. Int. Ed.* **2015**, 54, 10530 – 10534; *Angew. Chem.* **2015**, *127*, 10676 – 10680.
[22] X. Fan, H. Zhou, X. Guo, *ACS Nano* **2015**, *9*, 5125 – 5134.
[23] J. Tian, Q. Liu, A. M. Asiri, X. Sun, *J. Am. Chem. Soc.* **2014**, *136*, 7587 – 7590.
[24] H. B. Wu, B. Y. Xia, L. Yu, X.-Y. Yu, X. W. Lou, *Nat. Commun.* **2015**, *6*, 6512 – 6519.
[25] X. Zou, X. Huang, A. Goswami, R. Silva, B. R. Sathe, E. Mikmeková, T. Asefa, *Angew. Chem. Int. Ed.* **2014**, *53*, 4372 – 4376; *Angew. Chem.* **2014**, *126*, 4461 – 4465.
[26] M. Gong, W. Zhou, M.-C. Tsai, J. Zhou, M. Guan, M.-C. Lin, B. Zhang, Y. Hu, D.-Y. Wang, J. Yang, S. J. Pennycook, B.-J. Hwang, H. Dai, *Nat. Commun.* **2014**, *5*, 4695 – 4700.
[27] X. Lu, C. Zhao, *Nat. Commun.* **2015**, *6*, 6616 – 6622.

Received: March 3, 2016
Published online: April 21, 2016

